

Synthesis, physicochemical properties and visible light photocatalytic studies of molybdenum, iron and vanadium doped titanium dioxide

Hayat Khan · Dimitrios Berk

Received: 13 July 2013 / Accepted: 29 September 2013 / Published online: 17 October 2013
© Akadémiai Kiadó, Budapest, Hungary 2013

Abstract In this work, we use an inorganic titanium precursor (titanium oxysulfate, TiOSO_4) for the preparation of doped TiO_2 by the sol–gel method. Molybdenum (Mo), iron (Fe) and vanadium (V) in the concentration range of 0.0312–2.0 mol% are added as dopants. The prepared samples were characterized by XRD, FTIR, N_2 isotherms, SEM–EDX, TEM, UV–Vis DRS and PL techniques. X-ray diffraction revealed that an increase in the concentration of Mo causes the transformation of brookite into anatase phase. In contrast, Fe and V favor the formation of brookite phase. A decrease in crystallite size was observed on the addition of dopant ions compared to that of pure TiO_2 (7 nm), for 0.0312 mol% concentration of dopant in TiO_2 , a crystallite size of 6.3 nm (Mo), 6.2 nm (Fe) and 6.4 nm (V) was calculated. A noticeable change in anatase lattice parameter along the “c” direction was observed with increasing dopant concentration, this is evidence that the dopant ions have entered the TiO_2 crystal lattice by substitutional doping, which induces local distortion of the crystal structure and variation in interatomic distances. An increase in BET surface area and a decrease in pore size were observed with increasing dopant concentration, this may be due to their substitutional doping in crystal lattice and or their presence in the grain boundaries hindering the crystal growth. Diffuse reflectance studies indicate that doped TiO_2 showed visible light absorption compared to that of pure TiO_2 (3.1 eV). For 0.25 mol% concentration of dopant in TiO_2 , energy values of 2.6 eV (Mo), 2.95 eV (Fe) and 2.92 eV (V) were obtained. PL analysis clearly shows that the dopant ions have the capability to alter the oxygen vacancies and to produce Ti^{+3} surface species which trap the photogenerated electron and transfer the electron to surface absorbed oxygen and results in the decrease of electron hole pair recombination rate. Visible light photoactivity tests for the discoloration of methylene blue

H. Khan (✉) · D. Berk
Department of Chemical Engineering, McGill University, 3610 University street, Montreal,
QC H3A 2B2, Canada
e-mail: hayat.khan2@mail.mcgill.ca

demonstrated that the doped samples showed enhanced photoactivity compared to undoped TiO_2 and commercially available Degussa P25, because of composite nature, surface hydroxyl groups, narrowed band gap and decreased recombination rate of photogenerated electron–hole pairs. The highest photocatalytic activity was observed with 0.25 mol% dopant concentration, the calculated reaction rate constant (k_{obs}) was 0.97 min^{-1} (Mo), 1.18 min^{-1} (Fe) and 1.17 min^{-1} (V) compared to 0.18 min^{-1} (undoped TiO_2) and 0.17 min^{-1} (Degussa P25).

Keywords Titanium dioxide · Transition metals · Photocatalytic activity · Band gap · Recombination · Methylene blue

Introduction

Titanium dioxide (TiO_2) is an attractive material for a semiconductor photocatalyst, but it faces several drawbacks on large scale practical applications: (1) The wide band gap (3.2 eV) restricts the photocatalytic property to UV radiation (<390 nm), making it ineffective for visible light, and (2) the high rate of electron (e^-) and hole (h^+) recombination in TiO_2 tends to decrease its photocatalytic efficiency in degrading many of pollutants on its surface [1–3]. Therefore, to address these two main issues, a great deal of attention has been paid to the introduction of mid band gap cationic or anionic dopants into the TiO_2 crystal structure. In this respect, transition metals (Fe, Cr, Zr, V, Pt), rare earth metals (La, Nd, Ce, Er, Pr) and non-metals (N, F, S, Cl, Se, Br, I) were examined as dopants that improve the visible light photoresponse [3–5]. Liu et al. [6] reported that transition metals may introduce acceptor and/or donor levels in the wide forbidden band of TiO_2 . As a consequence, narrowing of the band gap occurs, and the photocatalyst responds to visible light. Transition metals exhibit variable oxidation states; because of this characteristic, when they are incorporated into the TiO_2 matrix, they may act as potential traps for photogenerated e^- and h^+ pairs preventing their recombination thus increasing their lifespan. Furthermore, transition metal ion doping may favor the formation of Ti^{+3} ions thus generating oxygen defects, as a consequence adsorption of oxygen to titania surface is facilitated and better photocatalytic activity is achieved [7].

Many research groups have prepared TiO_2 doped with transition metals (V, Fe, Cr, Mo and others) with the objective of lowering the band gap and to decrease the recombination rate for the attainment of enhanced photocatalytic activity in the visible range. However, the results found in the literature are often conflicting. For example, both Martin et al. [8] and Liu et al. [9] found that vanadium doping results in an enhanced charge carrier recombination rate, which reduces the catalyst photoactivity for 4-chlorophenol and methyl orange degradation. Li et al. [10] and Adan et al. [11] stated that presence of Fe as dopant in TiO_2 is detrimental for the photocatalytic degradation of organic contaminants in aqueous solution. Similarly, Litter and Navio showed that Fe(III)– TiO_2 results in slow degradation of toluene and benzaldehyde than pure TiO_2 [12]. In addition, controversial results are found in the literature about the role of Fe^{+3} ions in enhancing or decreasing the electron and

hole pairs recombination properties [13]. Moreover, according to Karakitsou and Verykios [14], the photocatalytic activity is enhanced by doping cations having a valance higher than Ti^{+4} , whereas Mu et al. [15] stated that doping TiO_2 with metal ions having an oxidation state of +3 or +5 act to decrease the photocatalytic activity. Thus, it is difficult to reach general conclusions on the effect of doping on TiO_2 band gap, charge carrier recombination rate and enhanced visible photocatalytic activity, because these are functions of particle size, crystalline phase and composition, synthesis method of doping and experimental conditions, as well as, nature and concentration of the dopant and titanium precursor.

Earlier works indicated that for the synthesis of transition metal-doped TiO_2 nanoparticles, the most common precursors were titanium alkoxides such as titanium isopropoxide, titanium butoxide and titanium ethoxide and an inorganic precursor such as titanium tetrachloride [3, 16–19]. These precursors are extremely sensitive towards moisture, heat and light, and they also possess the problem of undergoing very fast hydrolysis reactions during the synthesis of the catalyst. Thus, it is very difficult to control the physico-chemical properties of the final product. Also, titanium tetrachloride produces gaseous chlorine requiring special arrangements to control the production of this hazardous gas. There is no study in the literature to highlight the synthesis of doped TiO_2 with molybdenum, iron and vanadium from an inorganic titanium precursor, titanium oxysulfate by sol–gel method and also to illustrate the effect of different dopant ions on the physiochemical properties and surface features (photoluminescence analysis) of TiO_2 .

In this study, we report for the first time a modified, simple and environmentally friendly method for the synthesis of TiO_2 doped with different transition metals by a sol–gel route using titanium oxysulfate (TiOSO_4) as a precursor. The dopants molybdenum, iron and vanadium were selected, because their ionic radii (Mo^{+6} (0.62 Å), Fe^{+3} (0.64 Å) and V^{+5} (0.68 Å)) are smaller in comparison to Ti^{+4} (0.68 Å) in TiO_2 [6, 9, 16]. Hence, the substitution of these dopant ions may be possible in the crystal network. This will quench the overall band gap of the photocatalyst, leading to light absorption in the visible light region. We also consider the trends followed by crystallite size, specific surface area, porosity, phase composition, phase transformation, surface hydroxyl groups content and crystallinity as these properties play a vital role in heterogeneous photocatalysis.

Experimental methods

Materials

The following reagents were used as received from the suppliers: titanium oxysulfate TiOSO_4 ($\geq 29\%$ Ti (as TiO_2) basis, technical grade), nitric acid HNO_3 (volumetric, 2 M Fluka), ammonium molybdate tetrahydrate $(\text{NH}_4)_6\text{Mo}_7\text{O}_{24}\cdot 4\text{H}_2\text{O}$ ($\geq 99.0\%$ (T), BioUltra, Fluka), iron nitrate nanohydrate $\text{Fe}(\text{NO}_3)_3\cdot 9\text{H}_2\text{O}$ (99.99 % trace metal basis) and ammonium metavanadate NH_4VO_3 (99.996 % trace metal basis) all supplied by Sigma-Aldrich. Anhydrous barium chloride BaCl_2 (>97 %) and ammonium hydroxide NH_4OH (20 % v/v Ricca Chemical) were supplied by Fisher Scientific.

Synthesis of doped TiO₂ nanoparticles

The synthesis of doped TiO₂ is carried out by a modified sol–gel method [20] as follows: NH₄OH is added to 0.2 M solution of TiOSO₄ under constant magnetic stirring till the pH value reaches 7. After precipitation, the product titanium hydroxide (Ti(OH)₄) is separated through centrifugation and washed several times with deionized water to remove the free sulfate ions (confirmed by BaCl₂ test). The sulfate free precipitate is dispersed in deionized warm water, and HNO₃ is added till the sol attains a pH value of 2.0. Appropriate amounts of dopant solutions of (NH₄)₆Mo₇O₂₄·4H₂O for Mo–TiO₂, Fe(NO₃)₃·9H₂O for Fe–TiO₂ and NH₄VO₃ for V–TiO₂, were added dropwise to yield 0, 0.0312, 0.0625, 0.125, 0.25, 0.5, 1 and 2 mol% in the final solid product. The doped titania sol was dried in a water bath at 70 °C for 24 h, then pulverized to powder followed by calcination in a muffle furnace either at 300 °C or 500 °C, with 10 °C/min ramp and 1 h exposure time. The obtained pure and doped titanium dioxide photocatalyst were characterized as follows:

Morphological and structural characterization of the photocatalyst

XRD analysis was used to identify the crystalline phases, analyze their transformation and to measure the particle size and phase content. The diffraction patterns were recorded on a Phillips PW 1710 diffractometer using monochromatic high intensity Cu K_α radiation ($\lambda = 0.15418$ nm). The crystallite size (D) was calculated using the Debye–Scherrer formula (Eq. 1). The peak intensity of (101) of anatase and (121) of brookite reflections located at 25.4° and 30.8° on 2θ x-axis were used.

$$D = \frac{k \lambda}{\beta \cos \theta} \quad (1)$$

Here, k is a constant equal to 0.9, λ is equal to 1.5418 Å the X-ray wave length of Cu, β is full width at half maximum (FWHM) of the peak and θ is the Bragg's angle in radians. The phase contents of the samples were calculated using the following equations of Zhang and Banfield (Eqs. 2 and 3) [21].

$$\text{Anatase phase } \% = \frac{k_A A_A}{k_A A_A + k_B A_B} \quad (2)$$

$$\text{Brookite phase } \% = \frac{k_B A_B}{k_A A_A + k_B A_B} \quad (3)$$

where the coefficient k_A is 0.866 for anatase and k_B is 2.721 is for brookite; A_A , A_B , are the integrated intensities of the anatase (101) and brookite (121) peaks.

The lattice constants “a” and “c” for anatase ($a = b \neq c$) crystal system were determined from the two appropriate reflections, (101) and (200), using Eq. 4.

$$\frac{1}{d} = \frac{h^2 + k^2}{a^2} + \frac{l^2}{c^2} \quad (4)$$

where d is the lattice spacing, determined by Bragg's law in Eq. 5.

$$n\lambda = 2d \sin \theta \quad (5)$$

Fourier transform infrared spectroscopy (FTIR) spectra were recorded on a Bruker Tensor 27 with OPUS data collection program (V 1.1), in the energy range of 4,000–400 cm^{-1} . The sample was mixed with the reference potassium bromide (KBr).

Specific surface area and pore size distribution were determined by the BET (Brunauer–Emmett–Teller) and Barret–Joyner–Halender (BJH) methods, from nitrogen adsorption desorption isotherm at 77 K after degassing the sample at 200 °C for 2 h under nitrogen gas, using a Micromeritics TriStar analyzer.

The elemental composition of the doped sample was determined by scanning electron microscope (Hitachi S-4700 FE-SEM) attached EDX accessory operated at 2 kV and the catalyst particle size was recorded on transmission electron microscope (Phillips CM200 TEM) operated at 200 kV.

The band gap value of the photocatalyst sample was determined by diffuse reflectance spectra (DRS) which were obtained in the range 190–600 nm using a Thermoscientific UV–Vis Evolution 300 spectrophotometer equipped with an integrated Pike technologies EasiDiff, diffuse reflectance accessory. Potassium bromide (KBr) was used as a reference. The band gap analysis was done following the Kubulka-Munk function ($F(R)$), Eq. 6 [17].

$$F(R) = \alpha = \frac{(1 - R)^2}{2R} \quad (6)$$

where R is reflectance obtained as: $R = 10^A$, where A is the measured optical absorbance of the pure and doped semiconductor photocatalyst. The indirect band gap (ΔE_g) was measured by plotting $(\alpha h\nu)^{1/2}$ against $h\nu$ (photon energy) and the linear part of the spectra is extended to intersect the $h\nu$ axis (x-axis).

Photoluminescence (PL) spectra of the prepared samples were determined at room temperature with FluroMax-2 spectrofluorometer using the 350 nm line of Xe lamp as the excitation source.

The photocatalytic activity of the prepared samples was demonstrated in decoloration of methylene blue (MB) solution. The experiments were conducted in a cylindrical reactor containing 1.6 L aqueous solution of 6.25×10^{-2} g/L of the photocatalyst (pure or doped) and 8.75×10^{-3} g/L of MB. A 380 W Hg-medium pressure lamp (Heraeus Nobel Light, Germany) in the wavelength range of 310–660 nm with an intensity of 100 mW/cm^2 is used as a visible light source. The reacting mixture was bubbled continuously with external air under constant magnetic stirring, light illumination was supplied for a 6 min experimental duration. A sample of 2 ml was withdrawn at regular interval of 1 min. Before the UV–Vis analysis of the sample, it is filtered to remove the photocatalyst particles. The photocatalytic decoloration of MB was measured by following the decrease in its concentration with time, and the pseudo-first order reaction rate constant (k_{obs}) was determined by assuming first order kinetics and by plotting $\ln(C/C_0)$ versus time, where C_0 is the initial concentration of MB and C is the reaction concentration. For all the activity analyses, the maximum absorbance of MB at 662 nm was measured with a UV–Vis spectrophotometer.

Results and discussion

Phase identification, transformation and composition, crystallite size, crystallinity and lattice parameters

Fig. 1 illustrates the XRD patterns of pure and doped samples having the dopant Mo, Fe and V in the concentration of 0.0625 and 0.25 mol%, calcined at 300 °C. Marked on the figures are the main peak of the (101) plane of anatase and the (121) plane of brookite. The diffraction patterns of doped samples were similar to the pure TiO₂ sample. The only observed exception was for the sample having Mo concentration of 0.25 mol% (see Fig. 1. insert, e), showing the absence of the brookite (121) peak. This implies that increasing the concentration of molybdenum in the sample causes the inhibition of the growth of brookite or the transformation of brookite into pure anatase phase. As reported in the literature [16], iron allows the formation and growth of brookite phase. Similarly, the addition of vanadium favours the growth of brookite phase in the final product. However, this result is in contrast to that reported by Li et al. [18] who used titanium butoxide as titanium precursor. Moreover, in all doped samples, no diffraction peak was observed for Mo, Fe and V linked with Ti–O. This is the evidence that the dopants are uniformly dispersed in TiO₂ lattice, and XRD is not sensitive enough to record such minor changes to TiO₂. These results suggest that the substitutional interactions between

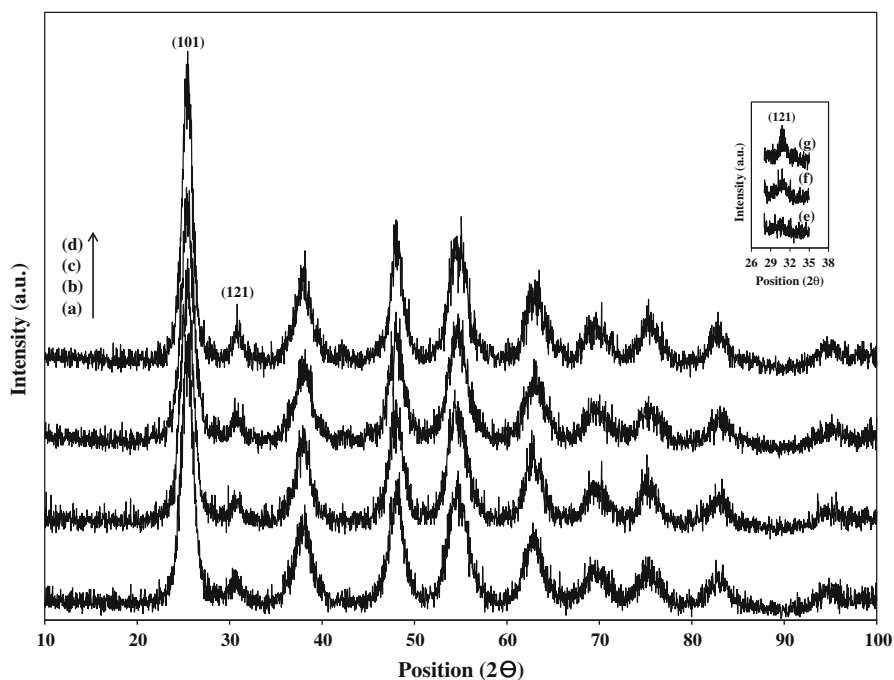


Fig. 1 XRD patterns of samples calcined at 300 °C; **a** TiO₂ and **b, c, d** 0.0625 mol% Mo, Fe and V in TiO₂. Insert **e** 0.25 mol% Mo (no brookite peak); **f, g** 0.25 mol% Fe and V (showing the (121) brookite peak)

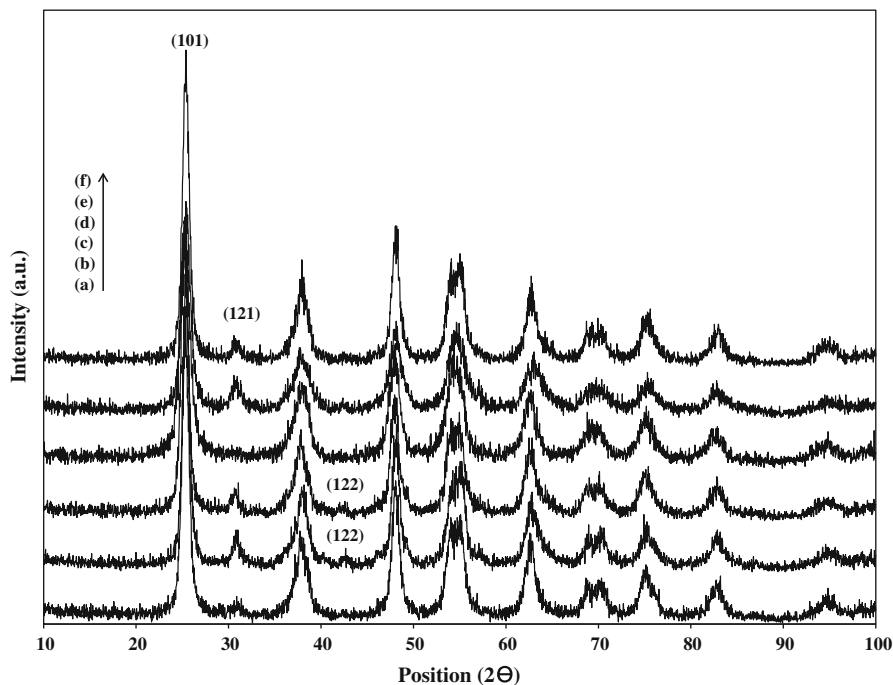


Fig. 2 XRD patterns of doped powder calcined at 500 °C; **a, b, c** 0.125 mol% Mo, Fe and V in TiO₂; **d, e, f** 1 mol% Mo, Fe and V-TiO₂

the dopant and titanium ions may play a significant role in phase transformations and will suppress the atomic rearrangement within a specific crystallographic plane. Moreover, they also cause the breakdown of Ti–O bonds in the TiO₆ octahedron unit; as a consequence different crystalline phases may be formed.

Fig. 2 shows the XRD patterns of the samples calcined at 500 °C. The (121) brookite peak persist up to 0.125 mol% concentration of Mo while Fe and V doped samples not only preserve this peak, but also a new peak (221) which belongs to brookite phase appears at 2θ position range of 48.2864°–48.2563°. The increase in the calcination temperature causes good ordering of the atoms positions, enhancement in crystallinity and the growth of the (221) peak of brookite phase. Moreover, the formation of (221) peak is hindered in the sample containing 2 mol% of Fe and 0.25 mol% of V concentration.

Table 1 shows the crystallite sizes and phase fractional compositions for all samples calcined at temperatures of 300 and 500 °C. A general observation is that an increase in dopant concentration causes a decrease in crystallite size implying that coagulation among the particles is hindered because of the presence and substitutional doping of the dopant ions in TiO₂ crystal lattice. In addition, the presence of brookite phase (especially in Fe and V doped samples) may obstruct the growth of anatase phase due to its different crystallographic structure.

Overall, smaller crystallite sizes were obtained for Fe doped samples in comparison to Mo and V doped TiO₂, calcined at the two calcination temperatures.

Table 1 Crystallite sizes and fractional compositions of pure and doped TiO₂ samples calcined at 300 and 500 °C

Pure TiO ₂ / Dopant	Dopant conc. (mol%)	Crystallite size, nm (fractional composition) at 300 °C		Crystallite size, nm (fractional composition) at 500 °C	
		Anatase	Brookite	Anatase	Brookite
TiO ₂		7.0 ± 1.1 (0.81)	6.8 ± 0.3 (0.19)	13.2 (0.84)	8.4 (0.16)
Mo	0.0312	6.3 (0.84)	7.0 (0.16)	11.5 (0.84)	8.7 (0.16)
	0.0625	6.3 ± 0.4 (0.83)	8.7 ± 0.7 (0.17)	17.2 (0.86)	8.7 (0.14)
	0.125	9.8 (1.00)		17.2 (0.92)	5.8 (0.08)
	0.25	13.8 ± 0.7 (1.00)		11.5 (1.00)	
	0.5	11.5 (1.00)		10.6 (1.00)	
	1	11.0 (1.00)		7.7 (1.00)	
	2	4.3 ± 0.5 (1.00)		6.3 (1.00)	
Fe	0.0312	6.2 (0.75)	5.7 (0.25)	10.5 (0.80)	9.5 (0.21)
	0.0625	6.3 ± 0.5 (0.76)	5.8 ± 0.4 (0.24)	10.6 (0.80)	10.0 (0.20)
	0.125	7.7 (0.80)	8.7 (0.20)	15.3 (0.78)	10.0 (0.22)
	0.25	6.9 ± 0.6 (0.82)	5.8 ± 0.6 (0.18)	13.7 (0.78)	11.6 (0.22)
	0.5	9.8 (0.78)	8.7 (0.22)	17.2 (0.73)	11.6 (0.27)
	1	6.3 (0.72)	8.7 (0.28)	9.8 (0.64)	13.9 (0.36)
	2	5.7 ± 0.4 (0.77)	5.7 ± 0.6 (0.23)	8.6 (0.72)	14.0 (0.28)
V	0.0312	6.4 (0.75)	8.7 (0.25)	19.7 (0.76)	11.6 (0.23)
	0.0625	12.8 ± 0.7 (0.72)	14.0 ± 0.9 (0.28)	17.2 (0.82)	11.6 (0.20)
	0.125	11.5 (0.72)	10.0 (0.28)	18.7 (0.82)	17.4 (0.18)
	0.25	9.9 ± 0.8 (0.78)	8.7 ± 1.2 (0.22)	17.2 (0.88)	8.7 (0.12)
	0.5	7.0 (0.85)	5.8 (0.15)	13.8 (0.88)	8.7 (0.12)
	1	6.9 (0.86)	5.8 (0.13)	11.1 (0.92)	7.0 (0.10)
	2	5.8 ± 0.5 (0.86)	5.8 ± 0.2 (0.14)	8.6 (0.93)	5.8 (0.73)

± shows the reproducibility of results

As shown in Table 2, the crystal lattice parameters for the doped samples calcined at 300 °C, the variation in lattice parameter “c” is considerable in comparison to the parameter “a = b”. This may be further evidence that the dopant ions have entered the TiO₂ crystal lattice by substitutional doping. In TiO₂, the ionic radius of Ti⁺⁴ is 0.68 Å, while for the present dopants Mo⁺⁶ is 0.62 Å, Fe⁺³ is 0.64 Å and for V⁺⁵ is 0.68 Å [6, 9, 16]. This suggests that the dopants ions are capable of replacing substitutionally the Ti⁺⁴ in the crystal lattice because of similarity in the ionic radii. This all suggest that substitutional doping has caused variations in interatomic distances [22] and as a result noticeable deformation in the c-axis lattice parameter is observed.

From these results it will be advantageous to produce doped composite (anatase–brookite) TiO₂ from the inorganic precursor (TiOSO₄) though the stated synthesis method for enhanced photocatalytic activity. The reason can be ascribed to the

Table 2 Lattice parameters of anatase phase, $a = b$ and c (Å) in doped samples calcined at 300 °C

Dopant conc. (mol%)	Mo		Fe		V	
	a	c	a	c	a	c
0.0625	3.79	9.32	3.79	9.27	3.79	9.33
0.125	3.79	9.45	3.78	9.41	3.78	9.57
0.25	3.80	9.29	3.79	9.25	3.78	9.45
0.5	3.79	9.52	3.78	9.26	3.79	9.48
1	3.81	9.54	3.79	9.41	3.78	9.36
2	3.81	9.59	3.80	9.37	3.79	9.56

synergistic effect due to catalyst polymorph nature and the presence of dopant ions, which are helpful to reduce the recombination phenomena.

FTIR spectra

Fig. 3 represents the FTIR spectra in the range, 4,000–400 cm^{-1} for pure and selected doped TiO_2 samples, calcined at 300 °C. The spectra show broad absorption peaks in the range of 1,630–3,450 cm^{-1} which may be assigned to the H–O–H bending vibration of physisorbed water and OH stretching vibration of hydroxyl group adsorbed on the surface of TiO_2 [23]. These surface hydroxyl groups are the main hole (h^+) scavengers; it means that the hydroxyl groups react with photoexcited holes on the surface of the catalyst to generate highly oxidative hydroxyl radicals (OH^\bullet) for the decomposition of organics, thus enhanced photocatalytic activity is expected [24, 25]. A peak at 1,360 cm^{-1} for pure as well for doped TiO_2 (0.0312 mol%) with little shifting toward higher frequencies is observed, which may be assigned to N–O stretching vibrations indicating the presence of NO_3^- ions, which may be due to the addition of HNO_3 during the acidification of the sol in the peptization step [26]. In the region of 1,000–400 cm^{-1} , all samples consist of broad bands, which contributed to the bending vibration band of Ti–O and O–Ti–O and to the stretching vibration of Ti–O–Ti. A peak at 2,927 cm^{-1} exists in pure TiO_2 which is indicative of OH groups representing a class of acidic hydroxyl of varied strengths [19]. However, this peak was suppressed in the doped TiO_2 samples. Moreover, no stretching bands in doped samples like Mo–O, Fe–O or V–O were observed. It is possible that such bending frequencies may overlap the Ti–O bending frequencies and hence were not resolved.

Fig. 4 indicates the FTIR spectra for the doped samples calcined at 500 °C, it is interesting to note that the spectra are similar to those shown in Fig. 1a except for the peak at 1,360 cm^{-1} (stands for NO_3^-) which vanished. The adsorbed nitrates volatilized during the treatment at this high temperature.

Textural properties: nitrogen adsorption–desorption isotherm

Nitrogen sorption isotherms of pure TiO_2 and Mo, Fe and V doped TiO_2 measured at 77 K and their textural parameters are shown in Fig. 5 and Table 3. All the samples show typical type IV adsorption–desorption isotherm with a hysteresis loop, which

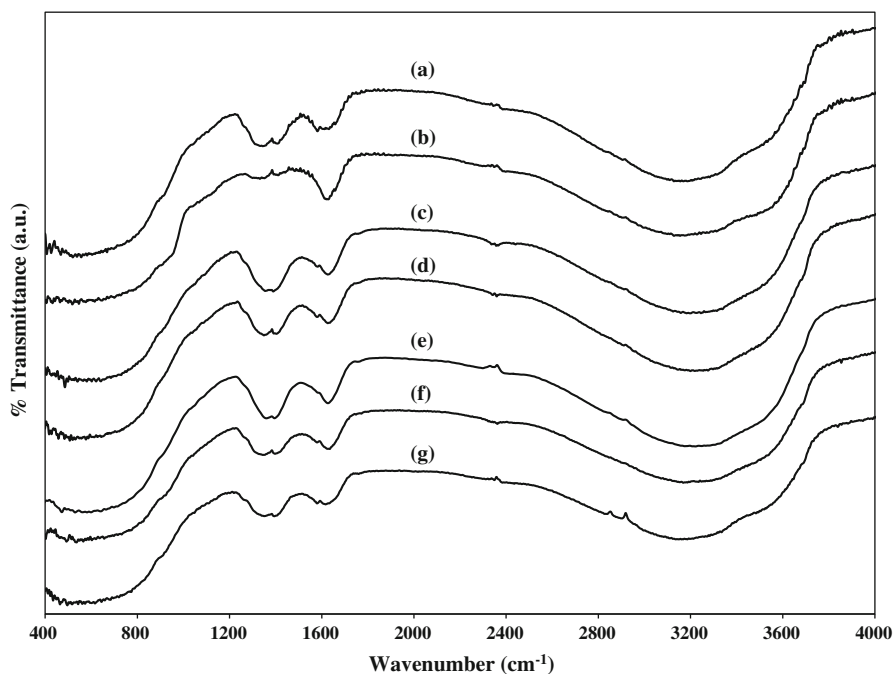


Fig. 3 Fourier transform infrared spectra of samples at 300 °C; **a** 0.0312 mol% Mo, **b** 1 mol% Mo, **c** 0.0312 mol% Fe, **d** 1 mol% Fe, **e** 0.0312 mol% V, **f** 1 mol% V and **g** TiO₂

indicates the appearance of mesoporous materials. The BET (Brunauer–Emmett–Teller) surface areas of the doped samples are lower than that of pure TiO₂. Furthermore, an increase in specific surface area and decrease in pore size is observed with increase in dopant concentration. This may happen because the substitutional doping in the crystal lattice hinders the crystal growth and due to excess dopant amount, its deposition in the grain boundaries causes the decrease in pore size. These results are consistent with the XRD data. A large surface area is desirable as it results in enhanced activity, but large crystal defects are usually associated with large surface area, which in effect favor recombination of photogenerated electrons and holes and thus resulting in lower activity [27]. The external surface area and BJH (Barret–Joyner–Halenda) desorption pore volume (for pores of diameter 17–3,000 Å) of pure and doped TiO₂ are also listed in Table 3. The S_{EXT} surface area of the samples is greater than the S_{BET} surface area. This implies that the solid contains micropores, which in aqueous solution are the major providers of adsorptive sites [28], thus promoting the adsorption of lower molecular weight and low concentration compounds to be decomposed in the photocatalytic process.

Microstructure and elemental composition analysis

The dopant ion concentration and the size of the doped catalyst particles were investigated by scanning electron microscope with attached energy dispersive X-ray

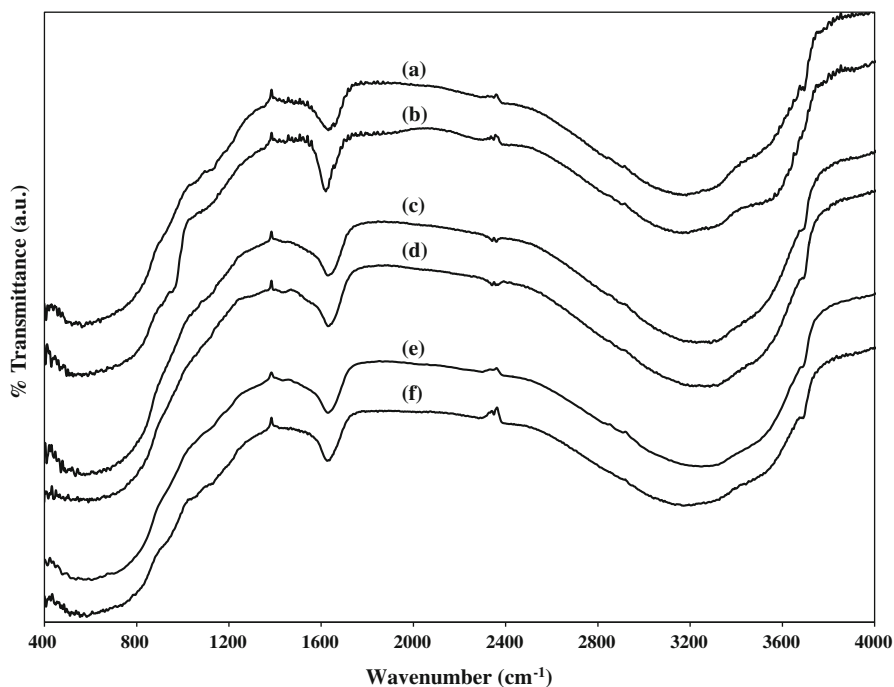


Fig. 4 Fourier transform infrared spectra of samples at 500 °C; **a** 0.0312 mol% Mo, **b** 1 mol% Mo, **c** 0.0312 mol% Fe, **d** 1 mol% Fe, **e** 0.0312 mol% V and **f** 1 mol% V

accessory (SEM–EDX) and transmission electron microscope (TEM). The EDX spectra of the doped samples displayed in Fig. 6 show the presence of the dopant in the synthesized TiO₂ nanoparticles whereas the XRD patterns (Sect. “Phase identification, transformation and composition, crystallite size, crystallinity and lattice parameters”) do not show any peaks related to Mo, Fe and V dopant ions. Therefore, this may be further evidence that the dopant ions are uniformly dispersed among the TiO₂ crystallites. The amount of the dopant metal ion with the main constituent Ti and O in both weight and atomic percent are displayed in the inserted table.

Figs. 7a, d, g represent the high magnification TEM images of the doped TiO₂ composed of highly ordered crystalline particles with minimum amorphous domains, which is an important prerequisite for good catalytic properties. Moreover, the particle sizes (shown in white rectangular box) are consistent with the XRD results, the inserted (b, e, h) crystal planes clearly indicate that of anatase structure. In the crystalline core, the d spacing corresponds to the lattice distance of the anatase [101] plane. The electron diffraction patterns (SAED) as shown in inserts (c, f, i) clearly indicates distinct rings, characteristics of highly order crystalline doped TiO₂ nanoparticles [6, 23].

Band gap measurements

The reflectance data spectra obtained was a relative percentage reflectance to a non-absorbing material (KBr) which can optically diffuse light. Table 4 shows the band

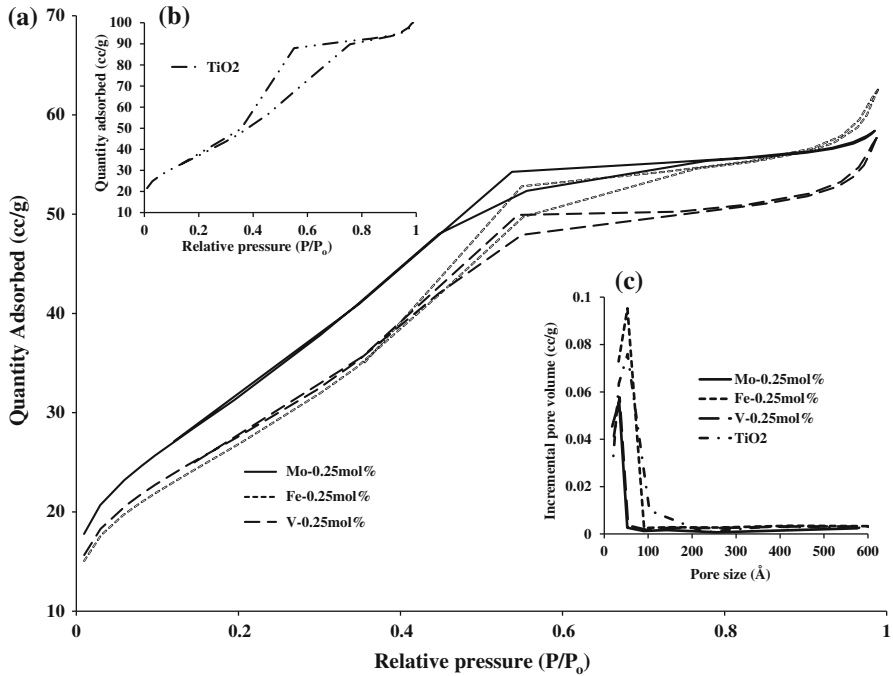


Fig. 5 Nitrogen adsorption–desorption isotherm for **a** 0.25 mol% Mo, Fe and V in TiO₂; insert **b** pure TiO₂; insert **c** pore size distribution

Table 3 Comparison of BET specific surface area, external surface area, pore size and BJH pore volume of pure TiO₂ and 0.25 and 2 mol% concentration of dopant Mo, Fe and V in TiO₂ samples at the calcination temperature of 300 °C

Pure/doped TiO ₂	S _{BET} (m ² /g)	S _{EXT} (m ² /g)	Pore size (Å)	BJH pore volume (cc/g)
TiO ₂	147	177	50	0.18
0.25 mol%-Mo	124	149	34	0.12
2 mol%-Mo	137	146	25	0.06
0.25 mol%-Fe	116	126	43	0.11
2 mol%-Fe	124	160	38	0.09
0.25 mol%-V	120	131	38	0.12
2 mol%-V	128	150	36	0.11

gap energies for all the samples and for some of the selected doped samples the Kubelka–Munk plots are shown in Fig. 8.

As presented in Fig. 8a, the presence of 0.125 mol% concentration of each dopant into TiO₂ caused a significant shift of the K–M spectra into the visible region compared to pure TiO₂. The obtained energy value of doped catalyst are 2.78 eV (Mo), 2.98 eV (Fe) and 2.97 eV (V), while for pure TiO₂ it is 3.1 eV. This reduction

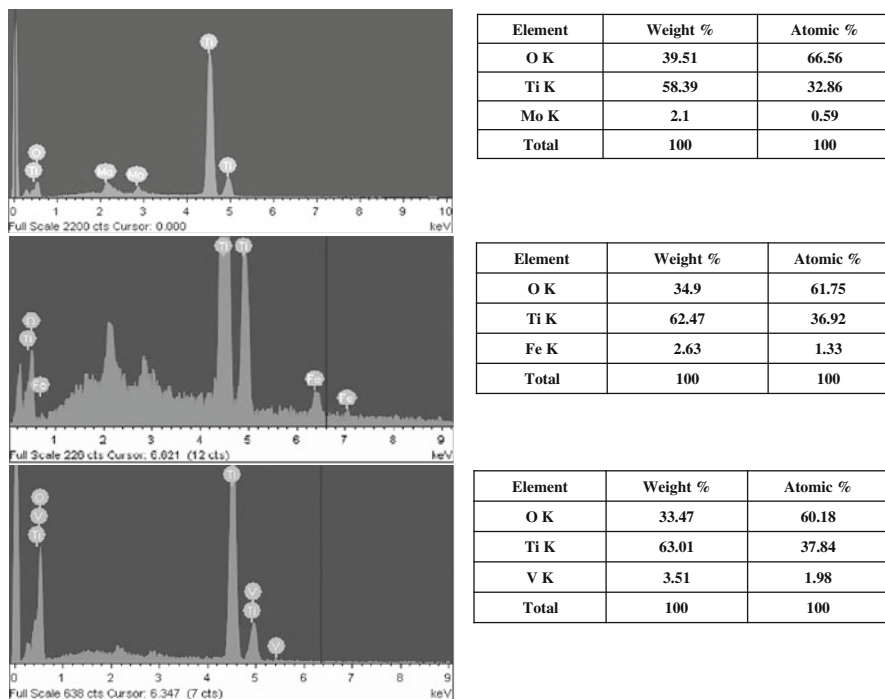


Fig. 6 SEM-energy dispersive X-ray spectra of 0.125 mol% concentration of doped samples; **a** Mo-TiO₂ **b** Fe-TiO₂ and **c** V-TiO₂; (insert tables) elemental composition analysis

in the band gap may be caused by the transition of electrons from the mid band gaps formed due to the addition of dopant in TiO₂ crystal lattice. In comparison, for pure TiO₂ the electronic transition is from O-2p valance band to Ti-3d conduction band.

There is an optimum amount of dopant that can be added to the catalyst with respect to the improvement of the visible light absorption. If the dopants exceed their solubility limit in TiO₂, they will be either deposited on the grain boundaries to accumulate and form clusters or they will precipitate in the interior of the crystallite. In either case they will not contribute to the change in the band gap. As shown in Fig. 8 (insert b), the 2 mol% concentration of Mo in the doped catalyst has higher band gap value than the 1 mol% concentration.

As illustrated in Table 4, the energy values decrease with increasing dopant concentration. In Mo doping, the Mo⁺⁶ has no electron in the d-orbital, this means the electronic transition from O-2p valance band will be enhanced to Mo sub energy level just created below the conduction band edge [19]. This new energy level, which is created below the conduction band of TiO₂, may be responsible for the activation of the catalyst under visible light illumination.

Evaluating the energy spectrum for Fe-TiO₂, a second absorption peak starts to appear at 480 nm (see Fig. 8 insert c), as the dopant concentration increases beyond 0.25 mol%. The first absorption threshold up to 460 nm may be accounted for some oxygen deficiency in the TiO₂ lattice [29] while the second threshold, starting from

Fig. 7 TEM images of 0.125 mol% concentration of doped samples **a, d, g** Mo, Fe and V in TiO_2 ; insert **b, e, h** crystal plane of anatase [101]; insert **(c, f, i)** SAED pattern. *Note: The numbers shown in the white rectangular box shows the individual particle size*

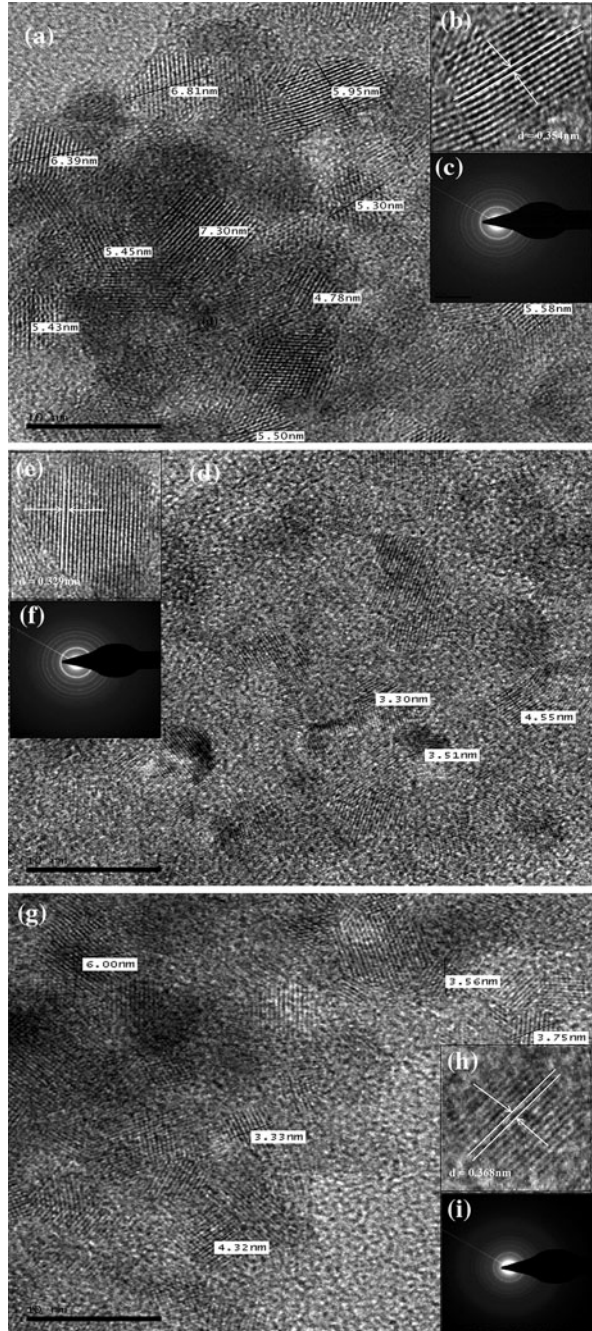


Table 4 Band gap energies of pure and doped samples calcined at 300 and 500 °C

Pure TiO ₂ /Dopant	Dopant conc. (mol%)	ΔE_g (eV) at 300 °C	ΔE_g (eV) at 500 °C
TiO ₂		3.10	3.04
Mo	0.0312	3.00	2.94
	0.0625	2.83	2.88
	0.125	2.78	2.8
	0.25	2.60	2.65
	0.5	2.55	2.60
	1	2.50	2.55
	2	2.63	2.60
	Fe	0.0312	3.07
0.0625		3.04	3.01
0.125		2.98	2.91
0.25		2.95	2.88
0.5		2.84	2.66
1		2.73	2.58
2		2.61	2.43
V		0.0312	3.00
	0.0625	2.98	3.00
	0.125	2.97	2.97
	0.25	2.92	2.91
	0.5	2.76	2.82
	1	2.70	2.70
	2	1.90	1.78

480 nm may be attributed to the substitution of Ti⁴⁺ atoms by Fe atoms. This suggests that incorporation of Fe ions into the lattice may form an impurity level just below the conduction band of TiO₂. As a result, the electron transfer will take place from the valance band to the dopant level or the transfer of 3d electron from ferric ions to the conduction band of TiO₂ or may be due to d–d transition [30] in the crystal field (electron transition between the two levels of five sp³d² hybrid orbital of ferric ions).

Fig. 8 insert c also illustrates that a noticeable increase in visible light absorption for V–TiO₂ is observed with increase in vanadium concentration. This may be due to the transition of charge from the valance band to the t_{2g} level of vanadium laying just below the conduction band of TiO₂ and or from the d–d transition of V 3d electrons (as indicated by the absorption band in the region 640–800 nm) [25]. Furthermore, it is evident that the slope of the absorption front decreases with an increase in vanadium concentration, our result are supported by Liu et al. [9].

Table 4 also demonstrates the band gap energy of the photocatalysts calcined at the temperature of 500 °C, the trend followed by ΔE_g is not straightforward. However, a small decrease in band gap is observed with an increase in the calcination temperature. This may be due to the increase in crystallinity of the

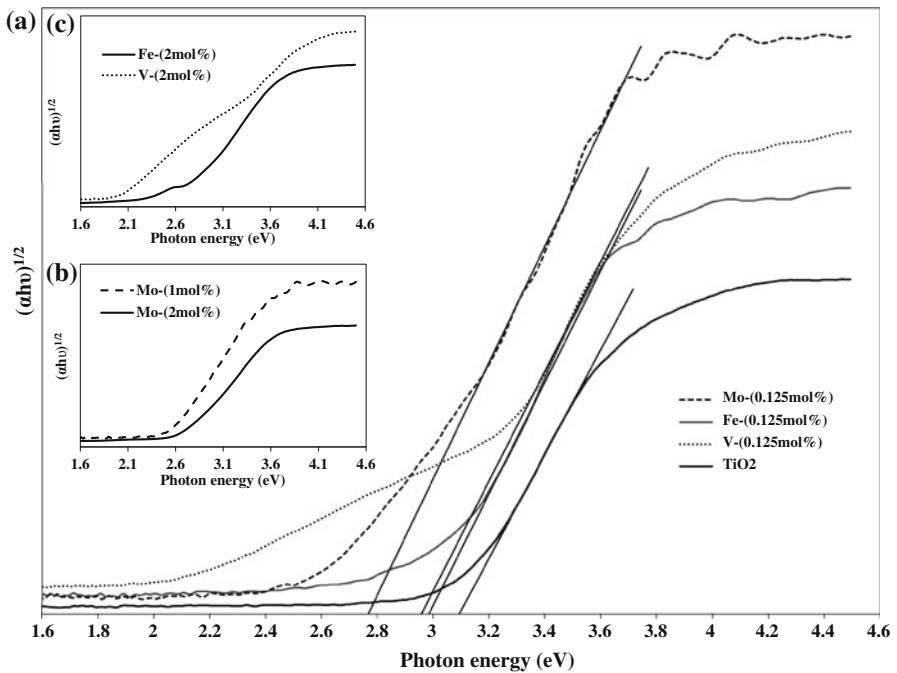


Fig. 8 Kubelka-Munk plots for **a** pure TiO_2 and 0.125 mol% Mo, Fe and V in TiO_2 ; insert **b** 1 and 2 mol% Mo- TiO_2 ; insert **c** 2 mol% Fe and V- TiO_2

sample. Moreover, all doped catalyst impart color due to the formation of energy levels by the dopants.

Comparing the doped catalyst samples, the order with decreasing band gap is Mo- $\text{TiO}_2 < \text{V-TiO}_2 < \text{Fe-TiO}_2$. This result illustrates that under the same synthesis conditions, the addition of Mo ions causes a much lower band gap of TiO_2 , which may be due to comparatively small ionic radius and high electronegativity value (2.16), means lower energy than vanadium (1.63) and iron (1.83).

Photoluminescence spectra and the recombination of electron-hole

Fig. 9 shows the photoluminescence (PL) spectra of pure and some selected doped photocatalyst. PL analysis helps in understanding the charge carrier trapping, migration and transfer because PL emission spectrum is the outcome of recombination of free carriers, i.e. electron and hole.

In the PL spectra shown in Fig. 9, the peaks at wavelength of 467 and 547 nm are attributed to an oxygen vacancy trapped electrons [31, 32], while the peak at 564 nm is proposed to correlate with a surface state (Ti^{+3}) [33]. These results clearly depict that Ti^{+4} substitution by the dopants induces the formation of oxygen defect states and Ti^{+3} surface species which may trap the photogenerated electrons and as well transfer the electron to surface adsorbed oxygen; as a consequence reduction in the recombination phenomena will occur. The peaks in the series 430,

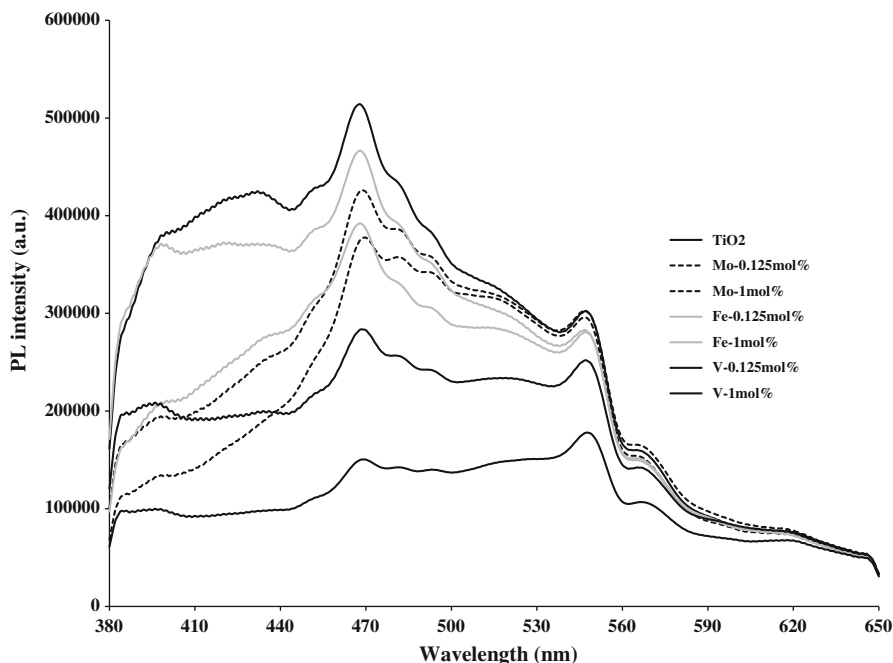


Fig. 9 Photoluminescence spectra of pure TiO_2 and 0.125 and 1 mol% Mo, Fe, V in TiO_2

450, 481 and 490 nm can be assigned to the formation of oxygen defects state (TiO_{2-x}) located near the bottom of the conduction band [34]. The UV emission peaks at lower wavelengths of 383 and 398 nm are ascribed to the direct transition of electrons from the valance to the conduction band [35].

Moreover, the PL spectra of doped TiO_2 showed a decrease in intensity as compared to the significantly stronger PL spectra of pure TiO_2 . It is obvious that the PL emission is the outcome of the recombination of excited electrons and holes, the lower the PL intensity, the lower the rate of recombination. Therefore, the decrease in the intensity of the PL spectra of doped materials indicated that the dopant Mo, Fe and V acts as trapping sites for either or both electrons and holes. These dopants successfully enhance the separation of e^- and h^+ and thus quench the photoluminescence. On the basis of this, enhanced photocatalytic activity for the doped samples can be expected. The efficiency of photocatalytic system is dependent on the transfer rate of photogenerated e^- and h^+ (e^- should reach the surface to react with externally supplied oxygen in the bulk to produce super oxide anions and h^+ should migrate to react with adsorbed pollutants or with surface hydroxyl groups to produce hydroxyl radicals) and inversely proportional to the rate of recombination. Fig. 8 also demonstrates that addition of V^{+5} ions in TiO_2 have resulted in greater decrease of PL intensity in comparison to Mo^{+6} and Fe^{+3} .

Furthermore, the PL emission peak intensities especially the ones at 467 nm decrease with an increase in dopant concentration indicating that irradiative recombination is weakened. Nevertheless there must be an optimum value for

dopant ion addition in TiO_2 , because excess increase in dopant concentration results in an increase in recombination of electron and holes [36].

Photocatalytic experiments

All doped catalysts showed significantly higher visible photoactivity than pure TiO_2 and the commercially available Degussa P25 catalyst, the photocatalytic experiments were repeated three times, the results with the highest activity are shown in Figs. 10, 11 and 12. The dopants not only act as trapping sites for both electrons and holes as already explained in PL analysis, but the dopants can also enhance the interfacial electron and hole transfer. As an outcome, the rate of recombination is decreased and visible photocatalytic activity is increased. Another reason, for such enhanced activity is the creation of oxygen defect states as a result of charge compensation when the dopant ions are substituted for Ti^{+4} in TiO_2 structure. The oxygen defect states are the main scavengers for the excited electrons.

It is well documented elsewhere [37, 38], that Mo and Fe dopants possess the capability of trapping both electrons and holes; this may be reason for their enhanced activity. However, in case of V, the t_{2g} level of V 3d orbit lies below the conduction band edge of TiO_2 , which can only capture the excited electrons [38].

We propose the following mechanism for V doped photocatalysis:

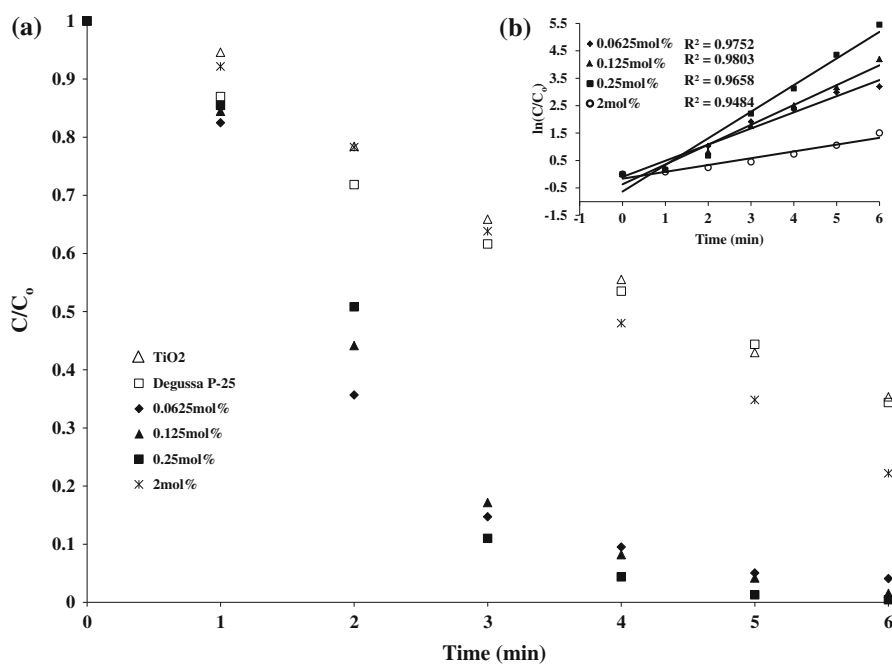


Fig. 10 Normalized degradation curves for methylene blue by **a** pure TiO_2 , Degussa P25 and different mol% of molybdenum (Mo) in TiO_2 ; insert **b** the plot of $\ln(C/C_0)$ versus time for the 0.0625, 0.125, 0.25, and 2 mol% Mo– TiO_2

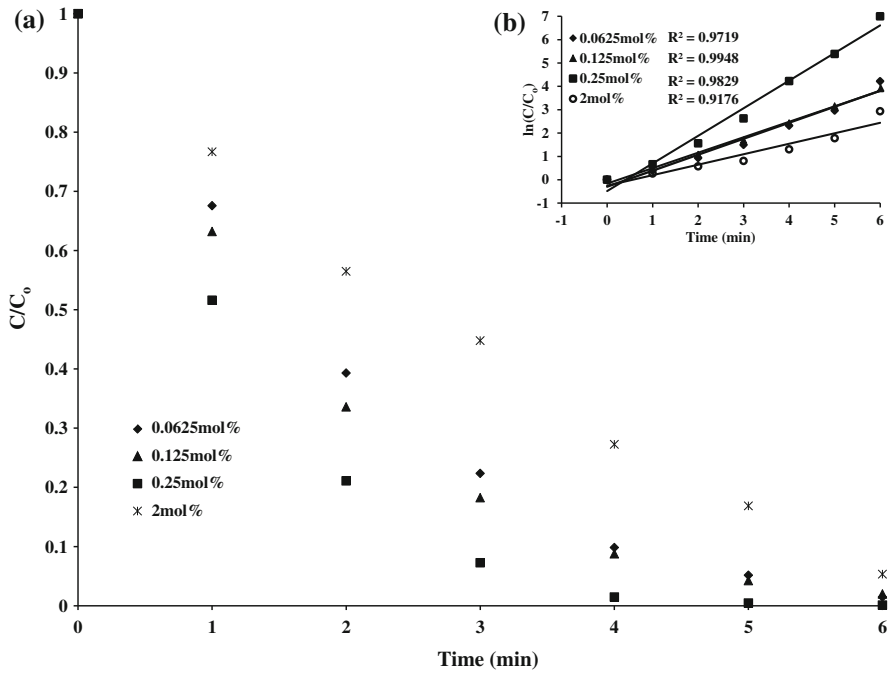


Fig. 11 Normalized degradation curves for methylene blue by different mol% of iron (Fe) in TiO_2 ; insert **b** the plot of $\ln(C/C_0)$ versus time for the 0.0625, 0.125, 0.25 and 2 mol% Fe- TiO_2



The trapping of e^- by V^{+5} species results in the formation of V^{+4} surface states. These V^{+4} species can be easily detrapped and can transfer the electron to the surface adsorbed oxygen to produce V^{+5} species and superoxide radical ions. This means that V^{+4} can indirectly act as a driving force for the regeneration of the V^{+5} species on the surface where it reacts with hydroxyl groups present on the surface of TiO_2 to generate hydroxyl radicals. These hydroxyl radicals act as hole scavengers which are necessary for the initialization of photocatalytic reactions. Therefore, V^{+5} doping increases the life time of photogenerated excitons and in response enhance the photocatalytic activity.

The photocatalytic activity for doped catalysts decreases with an increase in dopant concentration beyond the optimum value of 0.25 mol%, because the excess dopant ions occupy the grain boundaries as well deposit on the surface of the catalyst hindering the particle porosity. Thus the distance between the trapping sites is decreased (leads to increase recombination rate) and also the adsorption of the dye on the surface active site is reduced.

Table 5 shows that the pseudo-first order rate constant (k_{obs}) increases with increasing the concentration of dopant up to 0.25 mol%, after that a sharp decrease

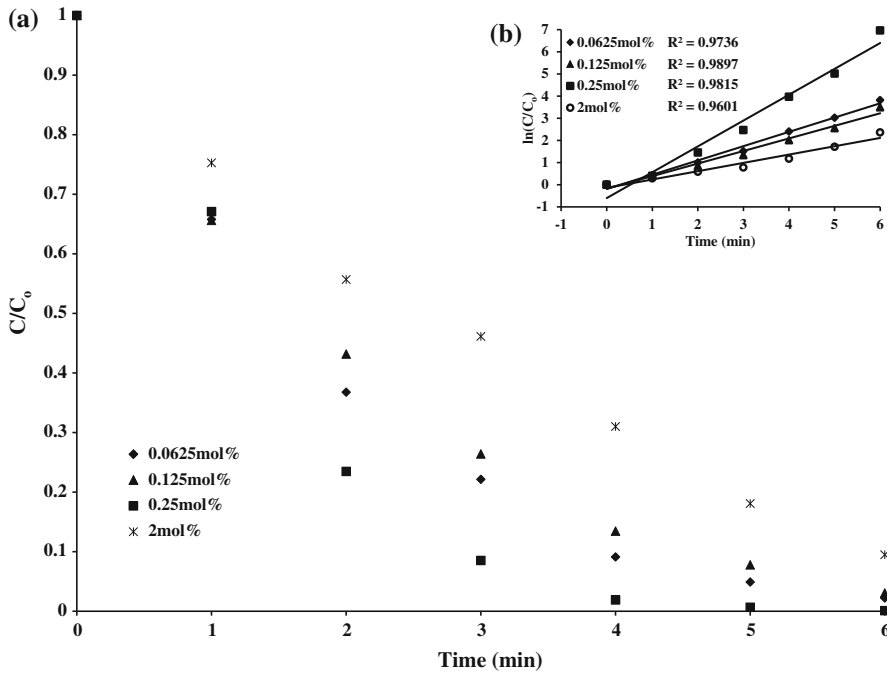


Fig. 12 Normalized degradation curves for methylene blue by different mol% of vanadium (V) in TiO_2 ; insert **b** the plot of $\ln(C/C_0)$ versus time for the 0.0625, 0.125, 0.25 and 2 mol% V- TiO_2

Table 5 Comparison of pseudo first order reaction rate constant (k_{obs}) of doped TiO_2 with increase in dopant concentration, powders were calcined at 300 °C

Dopant conc. (mol %)	Mo- k_{obs} (min^{-1})	Fe- k_{obs} (min^{-1})	V- k_{obs} (min^{-1})
0.0625	0.59 ± 0.05	0.69 ± 0.07	0.64 ± 0.05
0.125	0.72	0.66	0.57
0.25	0.97 ± 0.06	1.18 ± 0.04	1.17 ± 0.07
0.5	0.68	0.54	0.54
1	0.42 ± 0.04	0.51 ± 0.04	0.54 ± 0.03
2	0.25	0.45	0.38

± shows the reproducibility of results

in the trend is observed. The highest photocatalytic activity under visible light was observed with 0.25 mol% Fe doped TiO_2 , the calculated reaction rate constant (k_{obs}) was 1.18 min^{-1} (Fe) which is nearly 6.6 times higher than that of undoped TiO_2 (0.18 min^{-1}) and commercially available Degussa P25 (0.17 min^{-1}). Moreover, almost all of the MB photoreactions, Figs. 10, 11 and 12 (insert b) show the linearity (linear regression factor $R^2 > 0.9$), which indicates that MB decoloration follows pseudo-first order kinetics.

The photocatalytic activity of the doped samples calcined at temperature of 500 °C showed a decrease in visible photocatalytic activity. The Mo, Fe and V doped TiO₂ with dopant concentration of 0.125 mol% showed 60.5, 60.05 and 55.4 % percent decoloration of MB solution (not shown here). However, the band gap for these samples is somewhat similar to ones calcined at 300 °C, implying that the band gap is not the only cause of the improved activity. But, rather small crystallite size with high surface area and high degree of hydroxyl groups on the catalyst surface, which is expected to decrease and the rate of surface recombination increase with increase in calcination temperature, thus these may be the major reasons for such decrease in visible activity.

Conclusions

Pure and doped TiO₂ catalyst with different mol% concentration of molybdenum, iron and vanadium were successfully synthesized by a simple aqueous sol–gel method, using a cheap and easily handled inorganic precursor, titanium oxydisulfate. All the doped catalysts are composites of anatase and brookite, display a reduction in band gap by shifting the absorption profile to visible light region. Lower concentrations of Mo⁺⁶, Fe⁺³ and V⁺⁵ ions, in the range 0.0625–0.25 mol% in TiO₂, act as photogenerated electron–hole trapping centres that resulted in enhanced visible photocatalytic activity of the catalyst annealed at temperature of 300 °C when compared with pure TiO₂ and commercially available Degussa P25. Diffuse reflectance studies may suggest the substitutional doping of dopant ions for Ti⁺⁴ in TiO₂ crystal lattice while a decrease in the intensity of PL spectra with doping suggests the decrease in recombination of electron–hole pairs. The current study, which is the first of this kind, shows very active visible light photocatalyst been prepared by simple aqueous sol–gel route. This study will certainly offer great insight in practical application of Mo, Fe and V doped TiO₂ for heterogeneous photocatalysis of water treatment.

Acknowledgments Authors would like to acknowledge Brace Research Institute and the Natural Sciences and Engineering Research Council (NSERC) of Canada for the financial support provided for this work.

References

1. Bonsu PO, Liu X, Xie J, Jiang D, Chen M, Wei X (2012) *Reac Kinet Mech Cat* 107:487–502
2. Long R, English NJ (2011) *Appl Phys Lett* 98:142103–142106
3. Colmenares JC, Armendia MA, Marinas A, Marinas JM, Urbano JF (2006) *Appl Catal A* 306:120–127
4. Akpan UG, Hameed BH (2010) *Appl Catal A* 375:1–11
5. Ren G, Yuan Y, Liu X, Xing A, Liu H, Yin J (2010) *Reac Kinet Mech Cat* 100:487–497
6. Liu X, Geng D, Wang X, Ma S, Wang H, Li D, Li B, Liu W, Zhang Z (2010) *Chem Commun* 46:6956–6958
7. Kumar SG, Devi LG (2011) *J Phy Chem A* 115:12241–13211
8. Martin ST, Morrison CL, Hoffmann MR (1994) *J Phys Chem* 98:13695–13704
9. Liu B, Wang X, Cai G, Wen L, Song Y, Zhao X (2009) *J Hazard Mater* 169:1112–1118

10. Li Z, Shen W, He W, Zu X (2008) *J Hazard Mater* 155:590–594
11. Adan C, Bahamonde A, Garcia MF, Arias AM (2007) *Appl Catal B* 72:11–17
12. Litter MI, Navio JA (1996) *J Photochem and Photobiol A* 98:171–181
13. Piera E, Isabel TTM, Zorn ME, Anderson MA (2003) *Appl Catal B* 46:671–685
14. Karakitsou KE, Verykios EX (1993) *J Phys Chem* 97:1184–1189
15. Wei W, Herrmann JM, Pichat P (1989) *Catal Lett* 3:73–84
16. Popa M, Diamandescu L, Vasiliu F, Teodorescu CM, Cosoveanu V, Baia M, Feder M, Baia L, Danciu V (2009) *J Mater Sci* 44:358–364
17. Lopez R, Gomez R (2011) *Top Catal* 54:504–511
18. Li H, Zhao G, Chen Z, Han G, Song B (2010) *J Colloid Interface Sci* 344:247–250
19. Devi LG, Murthy BN (2008) *Catal Lett* 125:320–330
20. Sivakumar S, Pillai PK, Mukundan P, Warriar KGK (2002) *Mater Lett* 57:330–335
21. Zhang H, Banfield JF (2000) *J Phy Chem B* 104:3481–3487
22. Pal M, Pal U, Gracia JM, Jamenez Y, Rodriguez FP (2011) *J Nanoscale Res Lett* 7:1–12
23. Xiao J, Peng T, Li R, Peng Z, Yan C (2006) *J Solid State Chem* 179:1161–1170
24. Chen K, Jingyi L, Jie L, Zhang Y, Wang W (2010) *Colloid Surf A* 360:47–56
25. Music S, Gotic M, Ivanda M, Popovic S, Turkovic A, Trojko R, Sekulic A, Furic K (1997) *Mater Sci Eng B* 47:33–40
26. Carp O, Huisman CL, Reller A (2004) *Progr Solid State Chem* 32:33–177
27. Yuan R, Guan R, Zheng J (2005) *Scripta Mater* 52:1329–1334
28. Jing M, Wei Y, Liu WX, Cao WB (2009) *Res Chem Intermed* 35:329–336
29. Zhang J, Chen X, Shen Y, Li Y, Hu Z, Chu J (2011) *Phys Chem Chem Phys* 13:13096–13105
30. Li D, Haneda H, Hishita S, Ohashi N (2005) *Chem Mater* 17:2596–2602
31. Cong Y, Zhang J, Chen F, Anpo M (2007) *J Phys Chem C* 111:6976–6982
32. Chen SW, Lee JM, Lu KT, Pao CW, Lee JF, Chan TS, Chen JM (2010) *Appl Phys Lett* 97:012104-3
33. Lucovsky G (2007) *J Molec Struct* 838:187–192
34. Li FB, Li XZ (2002) *Chemosphere* 48:1103–1111
35. Zhou W, Liu Q, Zhu Z, Zhang J (2010) *J Phys D* 43:1–6
36. Devi LG, Kumar SG, Murthy BN, Kottam N (2009) *Catal Commun* 10:794–798
37. Tieng S, Kanaev A, Chhor K (2011) *Appl Catal A* 399:191–197
38. Tian B, Li C, Gu F, Jiang H, Hu Y, Zhang J (2009) *Chem Eng J* 151:220–227